Model-Based Despeckling and Information Extraction from SAR Images

Marc Walessa and Mihai Datcu

***Abstract*—Basic textures as they appear, especially in high resolution SAR images, are affected by multiplicative speckle noise and should be preserved by despeckling algorithms. Sharp edges between different regions and strong scatterers also must be preserved. To despeckle images, we use a maximum *a posteriori* (MAP) estimation of the cross section, choosing between different prior models. The proposed approach uses a Gauss Markov random field (GMRF) model for textured areas and allows an adaptive neighborhood system for edge preservation between uniform areas. In order to obtain the best possible texture reconstruction, an expectation maximization algorithm is used to estimate the texture parameters that provide the highest evidence. Borders between homogeneous areas are detected with a stochastic region-growing algorithm, locally determining the neighborhood system of the Gauss Markov prior. Smoothed strong scatterers are found in the ratio image of the data and the filtering result and are replaced in the image. In this way, texture, edges between homogeneous regions, and strong scatterers are well reconstructed and preserved. Additionally, the estimated model parameters can be used for further image interpretation methods.**

***Index Terms*—Bayesian inference, Gauss-Markov random fields (GMRFs), speckle noise, synthetic aperture radar (SAR), texture.**

I. Introduction

ALLOWING the acquisition of high resolution images of the Earth under all weather conditions, synthetic aperture radar (SAR) systems represent a very powerful observation tool. However, automatic interpretation of the information contained in the reflected intensity of the SAR data is extremely difficult [15]. These difficulties are due to the speckle phenomenon that can be regarded as a strong multiplicative noise affecting all coherent imaging systems. Since speckle strongly hinders data interpretation with standard image analysis tools, many filters have been developed to reduce speckle, e.g., [8], [10], [12]. Usually, these filters rely on simple model assumptions, i.e., stationarity of mean and variance, yielding fast and easily computable results. The filter equations are often equivalent to a weighted average of the original pixel value and an estimated mean. It is clear that this does not provide a satisfactory filtering of complex image structure even if some filters take into account nonstationarities of the mean backscatter by applying an edge detection step. Up to now, no filter is able to analyze and detect structure, or texture, in the image and to perform an adequate reconstruction.

Manuscript received September 16, 1999; revised March 22, 2000.

The authors are with the Remote Sensing Technology Institute (IMF), German Aerospace Center (DLR), Oberpfaffenhofen, D-82234 Weßling, Germany (e-mail: Marc.Walessa@dlr.de, Mihai.Datcu@dlr.de).

Publisher Item Identifier S 0196-2892(00)08900-2.

In this article, we propose a new Bayesian approach for speckle reduction in SAR images. The emphasis lies on speckle removal without losing textural and structural information which becomes more and more important in SAR image interpretation [16]. Strongly related to the task of despeckling are methods for SAR image segmentation and feature extraction yielding an algorithm for SAR information extraction.

Filtering SAR images, especially images of high resolution, requires a good preservation of textural features. As a consequence, textural properties contained in the image must be recognized to be accurately reconstructed in the filtered image [21], [22]. For this reconstruction we propose a new despeckling and information extraction algorithm (Fig. 1) that uses Gauss Markov random fields (GMRFs) as texture models and takes advantage of both the first and the second level of Bayesian inference to obtain a maximum *a posteriori* (MAP) estimate of the noise-free image. In the presence of noise, texture parameter estimation becomes a very difficult problem since the likelihood function of the noise must be considered. In order to obtain the best possible texture reconstruction, we propose an iterative algorithm to estimate the parameters that provide the highest evidence. These parameters are used to calculate the MAP estimate of the noise-free image. As a matter of fact, the employed Gauss Markov model is not sufficient to explain all SAR image features. For that reason, improvements are made by using information from additionally extracted features that can only be described by difficult to handle nonlinear models. These improvements contain the detection and preservation of strong scatterers and of borders between regions of uniform backscatter. While edges are preserved by an adaptive neighborhood system of the GMRF model, smoothed strong isolated scatterers are found in the ratio image of the noisy and the despeckled data and are reinserted in the image. This enables us to compensate for the shortcomings of a linear model while exploiting its advantages of easier tractability.

The article is organized as follows. In Section II, we shortly sketch the information theoretical aspects. After a short reminder of Bayesian inference, we present the likelihood function of speckle and the employed prior for texture reconstruction, which is the GMRF model. Then the general MAP solution for this model is derived, and the model parameter estimation is presented. In Section III, necessary model improvements are outlined. This comprises edge detection, together with model selection and the preservation of strong scatterers. Afterwards, the whole algorithm is briefly summarized. Results and examples are illustrated in Section IV. The developed algorithm is evaluated and compared to already

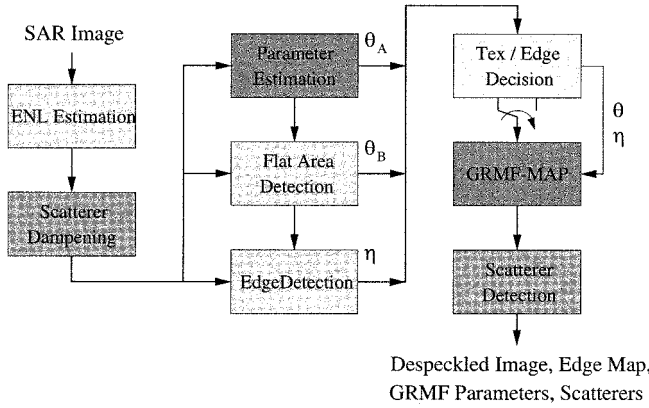

Fig. 1. Flowchart of the full model-based despeckling (MBD) and information extraction algorithm. After the eqivalent number of looks (ENL) estimation and the removal of strong scatterers, textural properties, flat areas, and edges are determined in the form of the parameters $\boldsymbol{\theta}_A$, $\boldsymbol{\theta}_B$, and η, respectively. This information is combined to generate a locally adaptive, edge- and texture-preserving MAP estimate. In a postprocessing step, blurred targets are detected and restored.

existing approaches using much simpler model assumptions. We conclude the article in Section V with a short summary.

II. Bayesian SAR Image Analysis

In order to filter out speckle, the rules of Bayesian inference [13], [20] are used, i.e., we try to estimate the noise-free image that best explains the noisy observation assuming some prior information. In our case, the prior comes in the form of a texture model. Using the Bayes equation at the first level of inference (the equation is given here for a single pixel, i.e., for local characteristics, which is justified by the Gibbs–Markov equivalence [5], [6]), we get

$$p(x|y,\boldsymbol{\theta}) = \frac{p(y|x,)\,p(x|\boldsymbol{\theta})}{p(y|\boldsymbol{\theta})}. \tag{1}$$

The following proportionality is found:

$$p(x|y,\boldsymbol{\theta}) \propto p(y|x,\boldsymbol{\theta})p(x|\boldsymbol{\theta}). \tag{2}$$

By x, we denote a noise free pixel of the image, y describes a pixel of the noisy observation, i.e., the SAR image, and by $\boldsymbol{\theta}$, we take into consideration the influence of a particular model or, more precisely, of the model parameters. (2) must be maximized as a function of x in order to obtain a MAP estimate. Concerning the likelihood function, we use the hypothesis $p(y|x,\boldsymbol{\theta}) = p(y|x)$ throughout the whole article.

Nonetheless, the power of the Bayesian approach lies in a second step, allowing us to choose the best model from a group of models. The same scheme applies for model parameters [3] and is, again, equivalent to computing the MAP estimate. Hence, assuming a uniform prior $p(\boldsymbol{\theta})$, we find an equivalent equation

$$p(\boldsymbol{\theta}|\mathbf{y}) \propto p(\mathbf{y}|\boldsymbol{\theta}) = \int p(\mathbf{y}|\mathbf{x})p(\mathbf{x}|\boldsymbol{\theta})\,d\mathbf{x} \tag{3}$$

where the integral must be performed over the whole space of $\mathbf{x}$ in order to obtain the so-called evidence. The vector notation for $\mathbf{x}$ and $\mathbf{y}$ denotes whole sets of pixels, e.g., $\mathbf{x} = (x_0, \cdots, x_{N-1})$.

A. Likelihood Function of Speckle

For SAR images, an assumed noise-free signal $\mathbf{x}$ is affected by speckle noise $\mathbf{s}$. This multiplicative noise, characteristic for coherent imaging systems, is of high variance compared to the mean image intensity. Unlike most approaches, we do not work on the intensity image since the used prior proved to be more suitable for amplitude images [23]. However, analytical calculations become more complex. The probability density function for the likelihood of the observed square root of the intensity $y = x \cdot s$ can be found to be [7]

$$p(y|x) = 2\left(\frac{y}{x}\right)^{2L-1} \frac{L^L}{x\Gamma(L)} \exp\left(-L\left(\frac{y}{x}\right)^2\right) \tag{4}$$

where L denotes the equivalent number of looks (ENL). For $L = 1$, the highest noise level is observed, and the noise variance decreases with L growing. For typical spaceborne SAR products, not considering single-look data, L is around three.

B. GMRF Texture Prior

To be able to preserve texture, we have chosen the GMRF model, which represents an autoregressive process, as our prior for $\mathbf{x}$ [17]. Although there are many more powerful nonlinear models, this model is used because of its better analytical tractability. The probability density function of the stochastic GMRF model is given by

$$p(x|\mathbf{x}_\eta,\boldsymbol{\theta}) = \frac{1}{\sqrt{2\pi\sigma^2}} \exp\left(-\frac{\left(x - \sum_{j\in\eta}\theta_j x_j\right)^2}{2\sigma^2}\right) \tag{5}$$

where θ_j and σ are model parameters describing textural information and the prediction uncertainty of the model, respectively. A neighborhood system around a central pixel x is denoted by η, and its size determines the complexity of the model. A precise description of neighborhood systems and orders can be found in [4], [18]. We employ the definition of the neighborhood system according to Fig. 2. In the following, we use the vector notation $\boldsymbol{\theta}$, with its dimension depending on the size of the considered neighborhood to denote the set of texture parameters θ_j and σ. Two realizations of GMRFs are shown in Fig. 3 with $\sigma = 4$ and $\boldsymbol{\theta} = (\theta_1, \theta_2, \theta_3, \theta_4) = (0.15, 0.45, -0.15, 0.05)$ (left) and $\boldsymbol{\theta} = (0.125, 0.125, 0.125, 0.125)$ (right), respectively. In the following, we also use the vector notation $\boldsymbol{\theta}$, with its dimension depending on the size of the considered neighborhood to denote the whole set of texture parameters θ_j and σ.

Linear autoregressive models are rather limited in their capability to describe complex features as will be illustrated in the next section. Nevertheless, complexity increases with model order, i.e., with the neighborhood size, and is found to be sufficient for a good number of textures contained in SAR images. The main drawback lies in the inability to model sharp transitions. To overcome this problem, we propose the use of an adaptive neighborhood system with model selection.

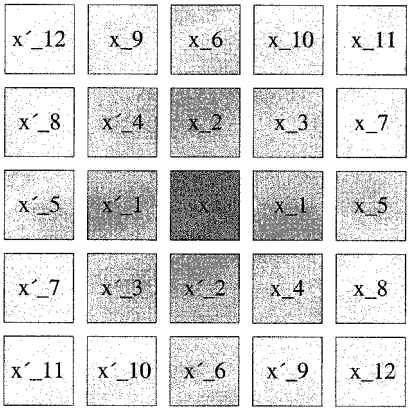

Fig. 2. Definition of the employed neighborhood system. Parameters θ_i are attributed to the pixel pairs x_i and x_i', which are symmetric with regard to the center pixel x. A third order model consists of six, a fourth order of ten, and a fifth order model of 12 parameters θ_i.

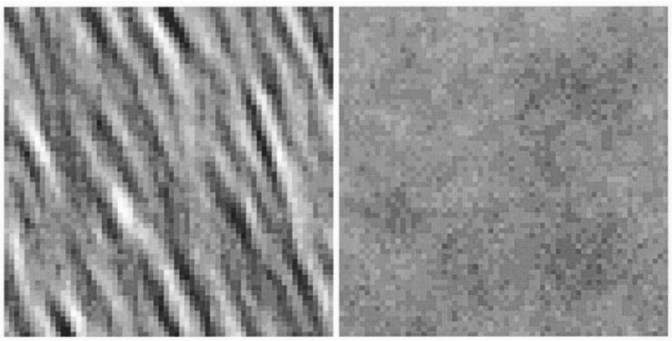

Fig. 3. Two typical example textures synthesized with different parameter sets of the third order, i.e., considering the 12 closest neighbors, GMRF model. Left: Typical wave or line structure. Right: Flat, isotropic texture.

C. MAP Solution for GMRFs

We use the likelihood function together with the chosen prior to calculate a MAP estimate of the noise-free scene $\mathbf{x}$. In a first step, we assume that the model parameters are already known. The parameter estimation is addressed in the next paragraph. Setting the first derivative of the logarithm of the posterior to zero

$$\frac{\partial}{\partial x}\log p(x|y,\mathbf{x}_\eta,\boldsymbol{\theta}) = -\frac{2L}{x}+\frac{2Ly^2}{x^3}-\frac{x-\sum_{j\in\eta}\theta_j x_j}{\sigma^2} = 0 \tag{6}$$

yields a fourth order polynomial (7) with four solutions for x_{MAP}, which depend on the model parameter vector $\boldsymbol{\theta}$ and the current neighborhood configuration of x denoted by η

$$x^4 - x^3\sum_{j\in\eta}\theta_j x_j + 2L\sigma^2x^2 - 2L\sigma^2y^2 = 0. \tag{7}$$

A valid solution for x_{MAP} must be real-valued and positive and can be found by a case study of the four possibly complex-valued roots. Because of interdependencies with unknown neighboring pixels x_j via $\boldsymbol{\theta}$, an iterative algorithm must be applied for relaxation [14]. In our case, a few iterations of a simple steepest descent algorithm with $\mathbf{x}=\mathbf{y}$ as initial guess provided good results. As demonstrated in Fig. 4, convergence to a stable solution is reached after three to five iterations.

D. Model Parameter Estimation

Knowing the solution for the MAP estimate of the noise-free signal given the parameters, the problem remains how to choose the values of the model parameter vector $\boldsymbol{\theta}$. To solve this problem, we take advantage of the second level of Bayesian inference to estimate the set of parameters that best explains the noisy image $\mathbf{y}$ for a given speckle noise level L [3]. Using the vector notation to consider a set of data within a window and assuming a uniform prior $p(\boldsymbol{\theta})$, we have to maximize the evidence given in (3). The integration must be performed over the whole space of $\mathbf{x}$, generally an unsolved problem for higher dimensions of $\mathbf{x}$, which depend on the estimation window size.

Note that the right-hand side of (3) is identical to the normalization constant neglected in (2). This term called evidence reflects the probability of the data $\mathbf{y}$ given an assumed model characterized by $\boldsymbol{\theta}$. The actual task consists in maximizing this evidence as a function of $\boldsymbol{\theta}$. This maximization is usually very difficult to perform, especially for non-Gaussian multidimensional functions that often occur in image processing. A closed analytical expression for the integral over the posterior $p(\mathbf{y}|\mathbf{x})p(\mathbf{x}|\boldsymbol{\theta})$ cannot be obtained. So several approximations are needed to make the problem tractable again, unless a computational, very demanding Markov Chain Monte Carlo (MCMC) means [11] is used. We make the following simplifications.

1) As a first approximation, the integrand of (3) is considered to consist of mutually independent random variables, breaking the joint probability density functions into the products of its components. Of course, this statistical independence is not given but has been shown to be a good approximation for large N, i.e., a large number of pixels within the estimation window, as it is similar to the maximum pseudo-likelihood approach presented in [9], [24].
2) Moreover, the multidimensional probability density function is approximated by a multivariate Gaussian distribution with Hessian $\mathbf{H}$, which is centered around the MAP estimate of $\mathbf{x}$, i.e., around the maximum of the posterior distribution [13], [20]. This can be shown to be a good approximation for the product of the likelihood function (4) and the Gauss Markov random field model (5). The quality of this approximation increases with growing values of L and decreasing σ [23].

Consequently, we find the Gaussian-shaped multivariate posterior

$$\begin{aligned} p(\mathbf{y}|\mathbf{x})p(\mathbf{x}|\boldsymbol{\theta}) &\approx \prod_{i=1}^{N} p(y_i|x_i)p(x_i|\mathbf{x}_{\mathbf{i}_\eta},\boldsymbol{\theta}) \\ &\approx \prod_{i=1}^{N} p(y_i|x_{i_{\mathrm{MAP}}})p(x_{i_{\mathrm{MAP}}}|\mathbf{x}_{\mathbf{i}_\eta},\boldsymbol{\theta}) \\ &\quad\cdot\exp\left(-\tfrac{1}{2}\,\boldsymbol{\Delta}\mathbf{x}^T\mathbf{H}\boldsymbol{\Delta}\mathbf{x}\right) \end{aligned} \tag{8}$$

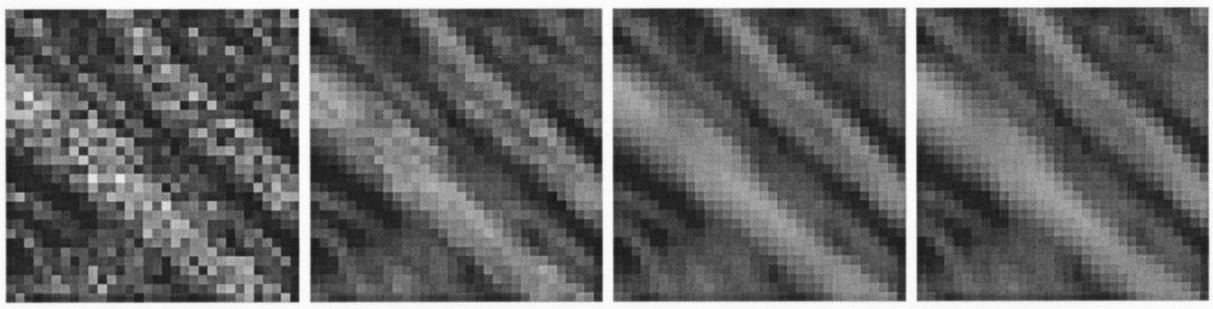

Fig. 4. From left to right: Evolution of the MAP estimate of $\mathbf{x}$ with known model parameters after zero, one, three, and five iterations using a steepest-descent algorithm.

where $x_{i_{\mathrm{MAP}}}$ is the MAP estimate of a pixel x_i obtained using a fixed parameter vector $\boldsymbol{\theta}$, $\boldsymbol{\Delta x} = \mathbf{x} - \mathbf{x}_{\mathrm{MAP}}$, and the Hessian matrix $\mathbf{H}$ is given by

$$\begin{aligned}\mathbf{H} &= -\boldsymbol{\nabla\nabla} \log \left(\prod_{i=1}^{N} p(y_i|x_i) p(x_i|\mathbf{x}_{i_\eta}, \boldsymbol{\theta}) \right) \Bigg|_{x_i = x_{i_{\mathrm{MAP}}}} \\ &= -\boldsymbol{\nabla\nabla} \sum_{i=1}^{N} \log(p(y_i|x_i) p(x_i|\mathbf{x}_{i_\eta}, \boldsymbol{\theta})) \Bigg|_{x_i = x_{i_{\mathrm{MAP}}}}. \quad (9)\end{aligned}$$

Applying these simplifications, we are now able to perform an integration of the approximating function

$$\begin{aligned}p(\mathbf{y}|\boldsymbol{\theta}) &= \int p(\mathbf{y}|\mathbf{x}) p(\mathbf{x}|\boldsymbol{\theta})\, d\mathbf{x} \\ &\approx \int \prod_{i=1}^{N} p(y_i|x_{i_{\mathrm{MAP}}}) p(x_{i_{\mathrm{MAP}}}|\mathbf{x}_{i_\eta}, \boldsymbol{\theta}) \\ &\quad \cdot \exp\left(-\tfrac{1}{2} \boldsymbol{\Delta x}^T \mathbf{H} \boldsymbol{\Delta x} \right) d\mathbf{x} \\ &\approx \frac{(2\pi)^{N/2}}{\sqrt{|\boldsymbol{H}|}} \prod_{i=1}^{N} p(y_i|x_{i_{\mathrm{MAP}}}) p(x_{i_{\mathrm{MAP}}}|\mathbf{x}_{i_\eta}, \boldsymbol{\theta}). \quad (10)\end{aligned}$$

Finally, since we prefer to use the logarithmic form of $p(\mathbf{y}|\boldsymbol{\theta})$ for numerical reasons, this can be expressed as

$$\begin{aligned}\log p(\mathbf{y}|\boldsymbol{\theta}) &\approx \tfrac{1}{2}(N \log 2\pi - \log |\mathbf{H}|) \\ &\quad + \sum_{i=1}^{N} \log p(y_i|x_{i_{\mathrm{MAP}}}) + \log p(x_{i_{\mathrm{MAP}}}|x_{i_\eta}, \boldsymbol{\theta}) \\ &\approx \sum_{i=1}^{N} \tfrac{1}{2}(\log 2\pi - \log h_{ii}) + \log p(y_i|x_{i_{\mathrm{MAP}}}) \\ &\quad + \log p(x_{i_{\mathrm{MAP}}}|x_{i_\eta}, \boldsymbol{\theta}) \quad (11)\end{aligned}$$

where h_{ij} are the components of the matrix $\mathbf{H}$. Another approximation was made in this final step

$$|\mathbf{H}| \approx \prod_{i=1}^{N} h_{ii}. \quad (12)$$

This approximation is assumed to be valid since it implies that all covariances resulting from this sparsely set matrix are zero (off-main-diagonal values are neglected), being in accordance with the already made inherent assumption of statistical independence in (8). Moreover, this simplifies practical calculations, preventing us from the computation of determinants of dimension $N \times N$, which are typically in the order of $21^2 \times 21^2$. In this way, we need only the components on the main diagonal of the matrix $\mathbf{H}$, which are found to be given by

$$\begin{aligned}h_{ii} &= -\frac{\partial^2}{\partial x_i^2} \sum_{j=1}^{N} -2L \log x_j - \frac{L y_j^2}{x_j^2} \\ &\quad - \frac{\left(x_j - \sum_{k \in \eta_j} \theta_k x_k \right)^2}{2\sigma^2} \Bigg|_{x_j = x_{j_{\mathrm{MAP}}}} \\ &= \frac{6L y_i^2}{x_{i_{\mathrm{MAP}}}^4} - \frac{2L}{x_{i_{\mathrm{MAP}}}^2} + \frac{1}{\sigma^2} \left(1 + \sum_{j \in \eta_i} \theta_j^2 \right). \quad (13)\end{aligned}$$

Being able to approximately compute the evidence, the final step for parameter estimation consists in finding the maximizing parameter vector. To achieve this, an expectation-maximization (EM) algorithm is used as outlined in Fig. 5 [3].

1) We start with an initial guess for $\boldsymbol{\theta}$, which corresponds to a uniform cross section, i.e., a pure amplitude average with $\theta_i = \kappa$ for all i, where κ is equal to 0.5/number of parameters θ_i.
2) E-Step: Using the current guess for $\boldsymbol{\theta}$, a first MAP estimate of $\mathbf{x}$ is calculated with (7).
3) The evidence for $\mathbf{x}_{\mathrm{MAP}}$ and $\boldsymbol{\theta}$ is computed using the approximations made above.
4) M-Step: Keeping $\mathbf{x}_{\mathrm{MAP}}$ fixed; a new $\boldsymbol{\theta}$ is iteratively chosen to maximize the evidence.
5) This procedure is repeated from step one with the new $\boldsymbol{\theta}$ until convergence is reached.

As a result, the maximum likelihood (ML) estimate of the parameter vector and the maximum *a posteriori* estimate of the cross section are obtained simultaneously. The evolution of the parameter estimates over several iterations of the EM algorithm is illustrated in Fig. 6.

III. Extraction of Nonlinear Model Features

GMRFs are good at describing a variety of smooth textures but perform poorly when sharp edges are to be preserved. In

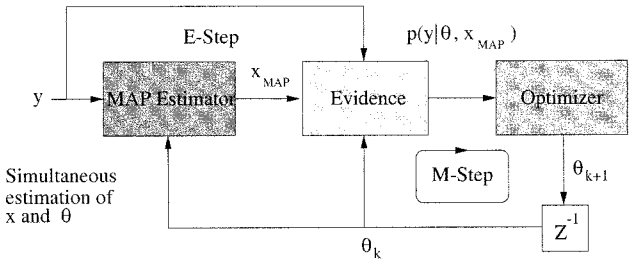

Fig. 5. Flowchart of the EM algorithm used for texture parameter estimation and MAP reconstruction.

general, the preservation of sharp edges requires the use of nonlinear models. Since we have chosen a linear model for practical reasons, a compound solution for this problem must be found. We use the GMRF model but extract nonlinear features with two algorithms to afterwards adapt the GMRF model accordingly or to do some other additional processing. Note that the GMRF does not require stationarity of the mean backscatter. Problems only arise for sharp transitions, i.e., high gradients of gray values.

To compensate for the smoothing effect at borders, we apply a local edge detection based upon a region growing algorithm. Found edges are used to adapt the neighborhood system η of the texture model, taking into account the nonstationarity of the signal. Another drawback of the GMRF model is that it cannot model small isolated features such as strong scatterer. Here, another solution is proposed: strong scatterers that are smoothed by the prior model are detected and put back in the filtering result after despeckling.

A. Local Edge Detection

Assuming a local area to be composed of r regions R_i with uniform backscatter values x_0 to x_{r-1}, the likelihood of the data can be written as [2]

$$p(\mathbf{y}|\mathbf{x}) = \prod_{i=0}^{r-1} \prod_{j \in R_i} p(y_j|x_i). \tag{14}$$

By maximizing this function, we segment the local area into r regions, giving us information about their borders as shown in Fig. 7. The maximization is performed by a region growing algorithm estimating $\mathbf{x}$ and attaching region labels to all pixels in a way that favors the formation of closed areas. The prerequisite for having uniformly labeled regions avoiding a noisy ML segmentation is determined by the updating scheme of the region growing technique. Starting with a random segmentation, the whole region under consideration, i.e., the local estimation window which has a typical size of 21×21 pixels, is scanned. The probability (14) of each border pixel to belonging to the class of a randomly chosen neighbor is calculated and compared to the probability of its current class. The decision is sampled from the resulting distribution and the estimates for x_0 to x_{r-1} are recomputed. After this, a number of iterations convergence is reached unless r is too high. Because we work locally on small areas, we set $r = 3$ in our algorithm assuming that the number of homogeneous regions is limited to that value. The quality of the final segmentation is independent of region shape and orientation.

B. Model Selection

After having applied the texture parameter estimation and the edge detection steps on local windows, different estimates $\mathbf{x}_{\mathrm{MAP}_j}$ of the cross section can be obtained, according to the following two assumptions.

1) We get a MAP estimate (7) using the extracted texture parameters without any information about edges, i.e., it is assumed that the noise-free image can be explained by the texture model alone.
2) The noise-free image is assumed to consist of several regions of different uniform backscatter. The image is filtered using (7), together with an adaptive neighborhood system at the region borders. The model parameters are set to values that cause a pure averaging of the amplitude image, i.e., $\theta_i = \kappa$ for all i, where κ is determined by the model order and the number of parameters.

Now one must decide whether to use the edge information and an adaptive neighborhood system or to use the unchanged texture model. The impact of this choice on the reconstruction is illustrated in Figs. 8 and 9 for an image without texture and a textured image, respectively. It is apparent that the correct choice is crucial. Texture must be preserved, but on the other hand, edges must not be smoothed by the GMRF model. The problem consists of finding out whether edges are due to texture as in Fig. 9, or if they are better explained by the assumption of homogeneous regions, as in Fig. 8. It is clear that edges are found in both images. However, for the reconstruction of the straw texture image, this information must not be used while it is indispensable for the chessboard image.

Since the evidence of the different models cannot be correctly evaluated, we adopted a different and much simpler approach to make this choice: The assumption of an area composed of different regions of uniform backscatter is verified by calculating the empirical coefficient of variation $\overline{y - \overline{y}/\overline{y}}$ and comparing it to the expected value for uniform regions. If a uniform area is detected, assumption two is used. Otherwise, assumption one is valid, leading to the corresponding reconstruction. We found this approach to work much better than approaches based on the likelihood or on the cross entropy [1] of the ratio image. Even for difficult cases, this approach yields the more correct reconstruction, as they are shown in Figs. 8 and 9, which is very important for a good visual appearance of the filtered image.

C. Preservation of Strong Scatterers

Strong scatterers highly disturb the parameter estimation of the texture model. The GMRF model is quite sensitive to small, especially linear features, which is usually its main advantage. Isolated targets, however, cannot be modeled by GMRFs. They require a nonlinear modeling. As a consequence, strong scatterers immediately affect the estimated parameters and influence the filtering of the whole surrounding area.

To circumvent this effect, we detect and remove point targets before parameter estimation to make the final estimate less

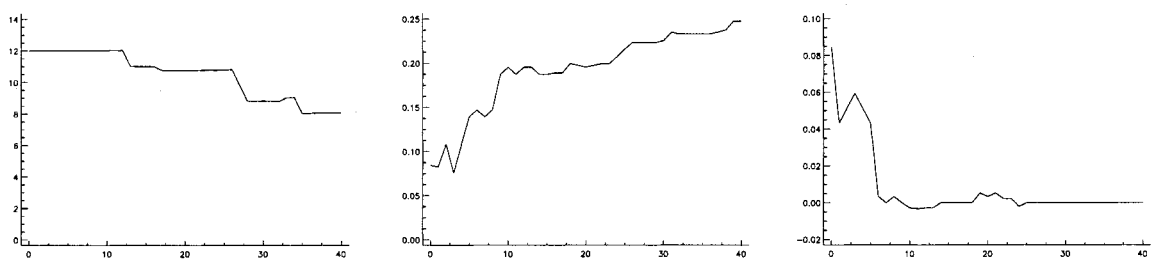

Fig. 6. Iterative EM estimation of the model parameters estimated from the image in Fig. 4. From left to right: Convergence of σ, θ_2, and θ_3 to their final estimates.

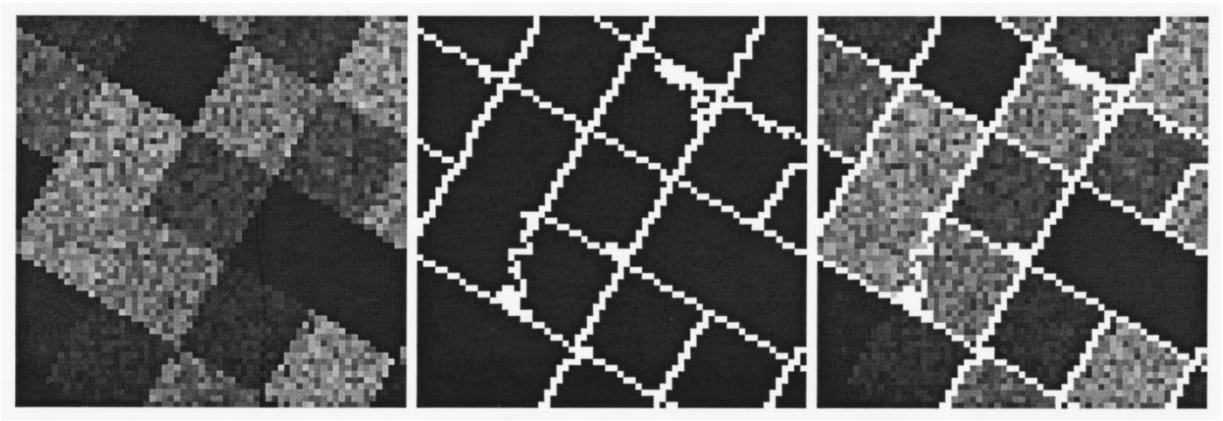

Fig. 7. Example for edge detection using the region growing algorithm. The original image is segmented into five classes. From left to right: Simulated noisy data, map of detected edges, and overlay of original data with edge map.

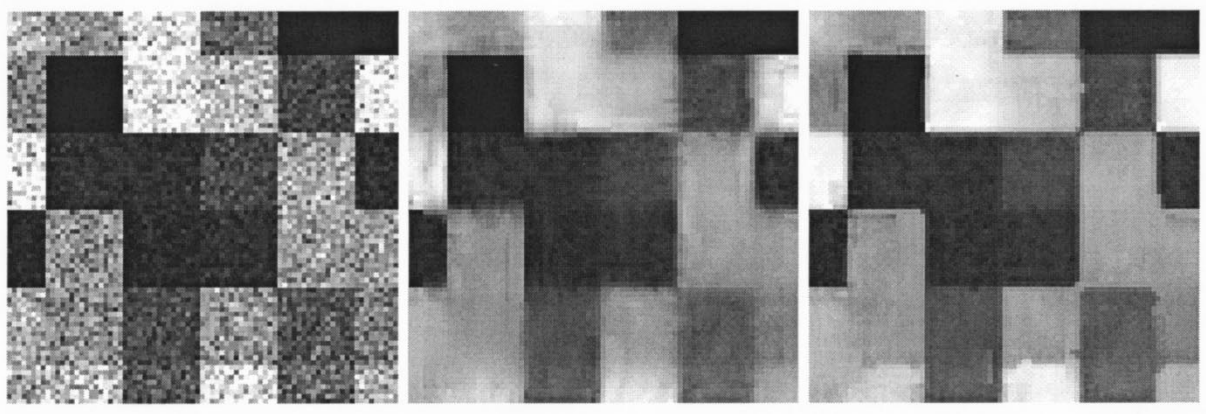

Fig. 8. From left to right: Untextured noisy data, data filtered without edge information, and data filtered with an adaptive neighborhood system under the assumption of uniform cross section. The right image gives a much better reconstruction.

sensitive to their influence. This can easily be done by calculating the ratio of the mean values of an inner and an outer window. The mean of the inner window is set to the one of the outer window if their ratio is beyond a statistically determined threshold [12]. Note that the algorithm may be this simple because only strong scatterers whose gray values do not lie within the range of the speckle distribution must be eliminated. Isolated points with lower gray values can be preserved. They only slightly, or not at all, disturb the parameter estimation, because they are interpreted as speckle. This indicates that the threshold is a function of the equivalent number of looks L.

Remaining strong scatterers, interpreted as noise, will be smoothed by the MAP despeckling. This requires a postprocessing step after filtering. Basically, all we really know is the speckle distribution. Therefore, failures of the filter are immediately apparent in the ratio image $\mathbf{y}/\mathbf{x}_{\mathrm{MAP}}$. This motivated the use of this ratio to detect smoothed scatterers. The original gray values are reinserted into the filtering result, where the value of the ratio image is out of the range of the speckle distribution, as depicted in Figs. 10 and 11. The threshold for the scatterer detection from the ratio image can be determined by fixing a constant false alarm rate.

One drawback of this approach must not be omitted. Scatterers that are not eliminated in the preprocessing step influence the filtering. Their intensity is spread around into neighboring pixels. As a result, the filtered image will have the original gray values of scatterers preserved but surrounded by a slightly brightened area.

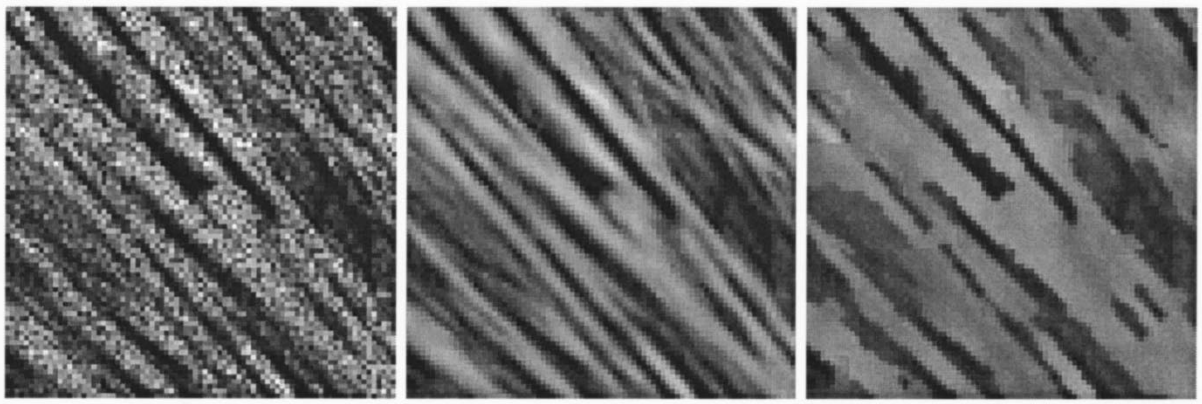

Fig. 9. From left to right: Textured noisy data, data filtered without edge information, data filtered with an adaptive neighborhood system under the assumption of uniform cross section. The center image gives a much better reconstruction.

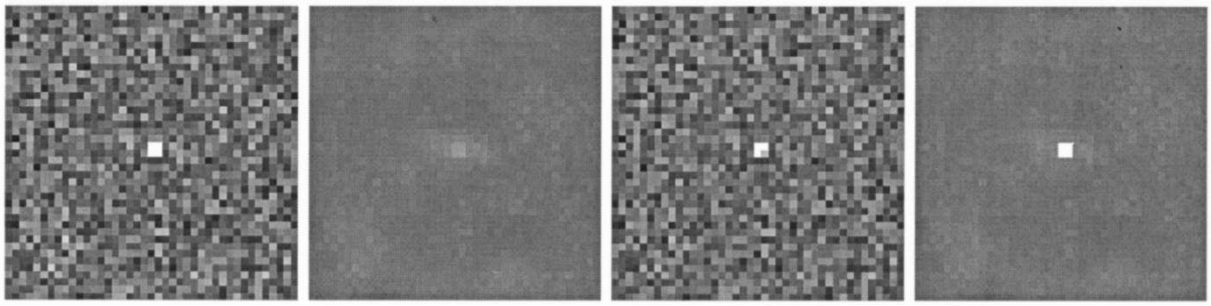

Fig. 10. Example for the detection of strong scatterers. From left to right: Noisy image including a strong scatterer, filtering result of the GMRF-MAP despeckling with the scatterer smoothed, ratio image $\mathbf{y}/\mathbf{x}_{\mathrm{MAP}}$ where the scatterer reappears, and final despeckling result with the detected strong scatterer included.

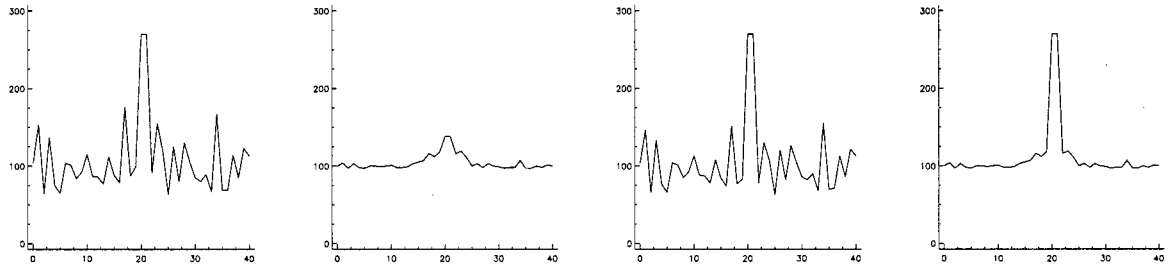

Fig. 11. Corresponding profiles for the images of Fig. 10. From left to right: Noisy strong scatterer, filtering result with the scatterer smoothed, ratio $\mathbf{y}/\mathbf{x}_{\mathrm{MAP}}$, and final result with the detected strong scatterer.

D. Model-Based Despeckling and Information Extraction

Before presenting several examples and comparisons in the next section, we summarize the algorithm called model-based despeckling (MBD), illustrated in the flowchart of Fig. 1.

1) The algorithm requires the speckled image as input and eventually the equivalent number of looks. Otherwise, L is estimated from the data.
2) Strong scatterers are detected and removed in order not to influence the model parameter estimation.
3) The model parameter vector $\boldsymbol{\theta}_A$ is estimated using a sliding or partly overlapping window. Typical window sizes used for texture detection are 21×21. From the point of view of stationarity, this is feasible, since due to the texture model, no stationarity of the mean backscatter is assumed as in most other filters. Neighborhood orders may range from two to ten. More than satisfactory results are already achieved with a fifth order model which is used in our algorithm.
4) Areas of uniform backscatter are detected using the coefficient of variation, and the edge detection is applied. The estimated value for σ of the GMRF is used for both the filtering of uniform and textured areas.
5) The correct model is chosen by an analysis of the extracted coefficients of variation, and the eventually modified parameter vector for flat areas $\boldsymbol{\theta}_B$, or the parameter vector $\boldsymbol{\theta}_A$, together with the appropriate neighborhood system, are used to calculate a MAP estimate of the noise-free image.
6) After despeckling of the full image, smoothed scatterers are detected by analyzing the ratio image $\mathbf{y}/\mathbf{x}_{\mathrm{MAP}}$ and are reinserted. The same applies for scatterers removed prior to filtering.

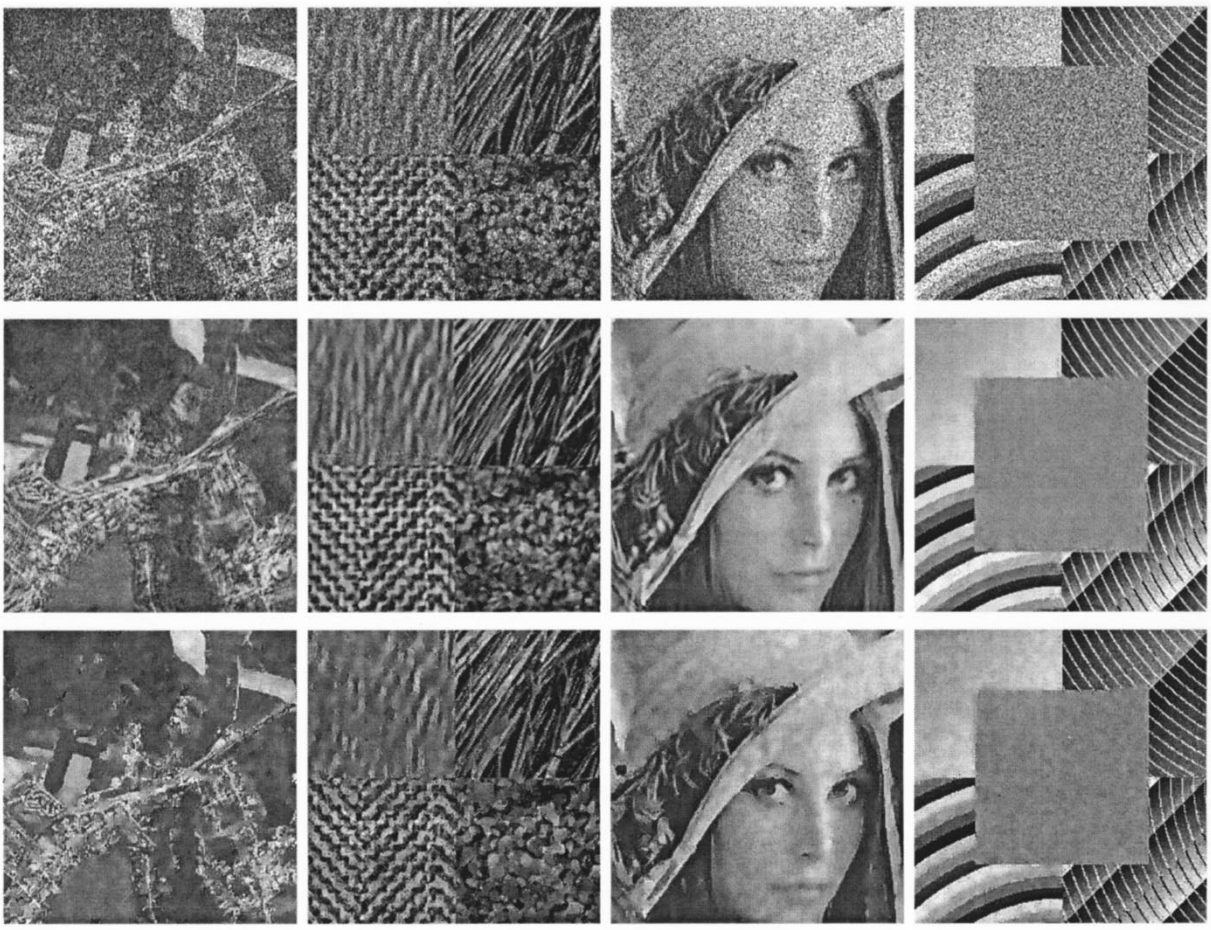

Fig. 12. (Top) Speckled, (Center) MBD-filtered, and (Bottom) GGMAP-filtered test images with very different contents used for speckle filter evaluation. The center parts (256 × 256 pixels) of the whole images (512 × 512 pixels) are shown. From left to right: Optical image, Brodatz textures, Lena image, and Synthetic image.

7) As a result, the filtered image, the estimated model parameters, an edge map, and the detected point targets are provided for further interpretation.

Because of the iterative EM algorithm employed for parameter estimation and the iterative computation of the MAP estimate, the whole algorithm is rather slow. This is also due to the calculation of the solution of the fourth order polynomial and the region-growing edge detection. In particular, the edge detection algorithm can be replaced by a standard method resulting in faster computation speeds. Using partly overlapping windows, the computation time for an image of 1024 × 1024 pixels is in the range of 30 min on a Pentium 300 machine.

IV. Results and Examples

In this section, we shortly present some results obtained with the described reconstruction and parameter estimation technique and make a comparison to other commonly used speckle filters. For test purposes, we present a quantitative evaluation using noiseless data where synthetic speckle has been added. In this way, we are able to compute several objective quality measures. For a pure visual evaluation, we show examples of real SAR images using X-SAR and high-resolution data filtered with the presented model-based despeckling (MBD) algorithm and provide an example application for the extracted information.

A. Synthetic Data Example

Four test images (Fig. 12) with very different contents are used in order not to restrict the performance evaluation to a certain image type. An optical image was chosen because of its similar scene contents compared to SAR images. To test the texture preservation, we generated an image consisting of four Brodatz textures. As a test for the model selection, the Lena image is taken since it comprises flat areas, edges, and texture. Finally, a pure synthetic image is used to verify the smoothing performance, the edge preservation, and the reconstruction of fine details, such as lines.

We tested the most frequently used filters, like the GGMAP [12] with edge detection (window size 7 × 7), the basic Lee filter [10] (window size 7 × 7), the EPOS filter [8] (window size 7 × 7), and a simple wavelet-shrinkage method, and compared the results to the proposed MBD-Filter. All test images are affected by synthetic 3-look speckle noise.

The following quality measures have been used for the filter comparison given in Table I.

1) MSE: Mean-square error between the filtered image and the original noise-free data.
2) Mean: Square-root of the mean intensity of the filtered data to be compared to the value of the original data denoted by μ.

TABLE I
QUANTITATIVE FILTER EVALUATION FOR TEST IMAGES 1–4. BEST VALUES IN EACH CATEGORY ARE DISPLAYED IN BOLD LETTERS

1. $\mu = 109$	MBD	GGMAP	LEE	EPOS	WVT
MSE	**309**	399	346	483	448
Mean	**103**	**103**	**103**	101	98
ENL	163	**175**	124	78	23
Speckle	4.5	**3.5**	4.6	3.6	3.7
2. $\mu = 090$	MBD	GGMAP	LEE	EPOS	WVT
MSE	**188**	375	331	449	448
Mean	**87**	**87**	85	85	78
ENL	60	**62**	31	20	22
Speckle	**3.3**	4.4	6.2	4.0	
3. $\mu = 133$	MBD	GGMAP	LEE	EPOS	WVT
MSE	**74**	133	166	215	378
Mean	**130**	127	127	125	123
ENL	**1020**	233	177	252	25
Speckle	**3.3**	3.8	4.0	3.4	4.6
4. $\mu = 125$	MBD	GGMAP	LEE	EPOS	WVT
MSE	**234**	280	405	390	816
Mean	**123**	119	119	116	110
ENL	**1390**	292	192	204	86
Speckle		4.5	5.0	**3.5**	

3) ENL: Maximum smoothing in the filtered image measured in a window of $35\times$ 35 pixels.
4) Speckle: Equivalent number of looks of the whole ratio image $\mathbf{y}/\mathbf{x}_{\boldsymbol{filtered}}$. This measure should be close to three. If the number is omitted, the measured value is lower than three, indicating strong filter-induced distortions, usually at borders or strong scatterers.

We notice that the model-based despeckling approach dominates in many categories, especially in the MSE and the smoothing performance. This can be explained by its superior modeling, which is not relying on simple averaging based on a mean/variance analysis but on the detection and reconstruction of features. In order to verify the preservation of structural information, we depict the ratio image scaled between 0.5–1.5 of the noisy data to the filtering results in Fig. 13 and compare the MBD to the GGMAP filter, which gave the best results for the used test images. Especially for the Brodatz image, considerably less structural degradation can be observed.

Unfortunately, it is impossible to verify, if the same favorable behavior of the MBD filter also applies for real SAR data since the made model assumptions might not be fulfilled. A universal quality measure for filtered SAR data, which could help to make this verification, does not exist.

B. High-Resolution SAR Data

Two small parts of high-resolution SAR data are shown in Fig. 14. Here the performance of the filter is clearly visible, e.g., in the reconstruction of the bright lines and the strong smoothing of the homogeneous areas. Also note the reconstruction of the upper right part of the leftmost image where a lot of structure is visible. Compared to typical satellite SAR image products the noise level in this example is much lower with ENL $= 8$. This yields a better estimate of the texture parameters, hence, a better reconstruction than for 3-look images.

C. Information Extraction from X-SAR Data

In Fig. 15, an example for X-SAR (Space Radar Lab, 1994) data is given. The visual quality of the despeckled image is rather high and similar to an optical image. Disturbing speckle is completely filtered out, edges are nicely preserved in the agricultural areas, and linear structures are well reconstructed by the GMRF model. A similar example is displayed in Fig. 16. The mountain ranges are well explained by the texture model, yielding a good reconstruction. Marked areas denote regions of high scatterer density, interpreted as urban areas. The interpretation was done based on the scatterer map provided by the algorithm. Having applied this processing on a couple of X-SAR scenes over Switzerland, this technique proved to be very robust. Almost no misinterpretations due to layover occurred.

In Fig. 17 a global segmentation of the same X-SAR image into five classes can be seen on the left. The result was obtained by the presented region growing technique, this time working globally on the whole image. An application for the extracted texture parameters is demonstrated on the right. The clustered norm of the parameter vector $|\boldsymbol{\theta}|$ without σ is displayed. Different regions of the image can easily be distinguished in the false-color overlay. Applying a GMRF parameter estimation without considering noise (resulting in a least-mean squares estimation) either on original or on conventionally filtered data, gives only a meaningless noisy clustering. This estimation is very sensitive to both remaining noise and filter-induced artifacts. Thus, the likelihood function must be considered for parameter estimation from noisy data, as in (11).

V. CONCLUSION

A new texture preserving despeckling algorithms has been presented that does not require any parameter tuning. Though computationally rather demanding compared to conventional despeckling techniques, even larger scenes can be processed within reasonable time, i.e., within a few hours. Unfortunately, the texture reconstruction may give unsatisfactory results in the case of correlated speckle since the noise correlation is not considered in the likelihood function. This problem can be solved by subsampling the data at the cost of reduced spatial resolution or by a model change. The latter is still under investigation. For low speckle correlation, the results of the proposed filter are generally of very high quality, especially where the reconstruction of texture, a strong smoothing and the preservation of edges is concerned. Concerning single-look SAR data, the quality of the filtering result and the estimated texture parameters is reduced. Only very strong textures can be captured in this case since the SNR is too low. The assumption of a Gaussian-shaped posterior still holds, although the accuracy is decreased. For products of three and more looks. However, the image quality increases significantly.

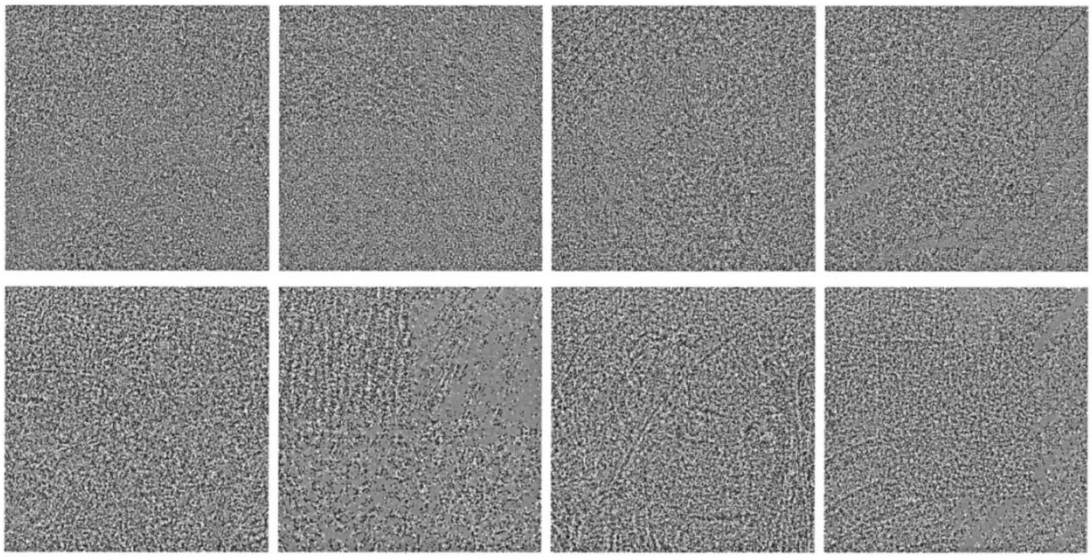

Fig. 13. Corresponding ratio images of the speckled data and the filtering results of Fig. 12 are displayed (top row: MBD filter, bottom row: GGMAP filter). From left to right: 1— Optical image, 2—Brodatz textures, 3—Lena image, 4—Synthetic image.

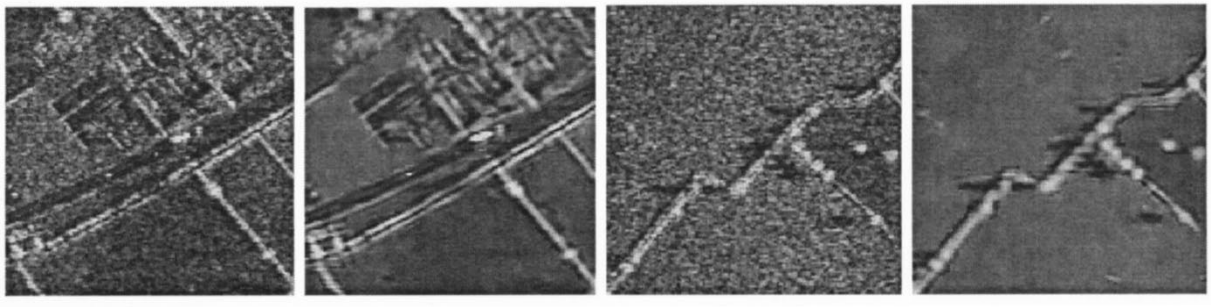

Fig. 14. High-resolution SAR image example. Left image of image pairs: Original SAR data (ENL $= 8$, 160×160 pixels) by N. A. Software, Ltd. Right image of image pairs: MBD-filtered data (ENL $= 98$ and ENL $= 157$).

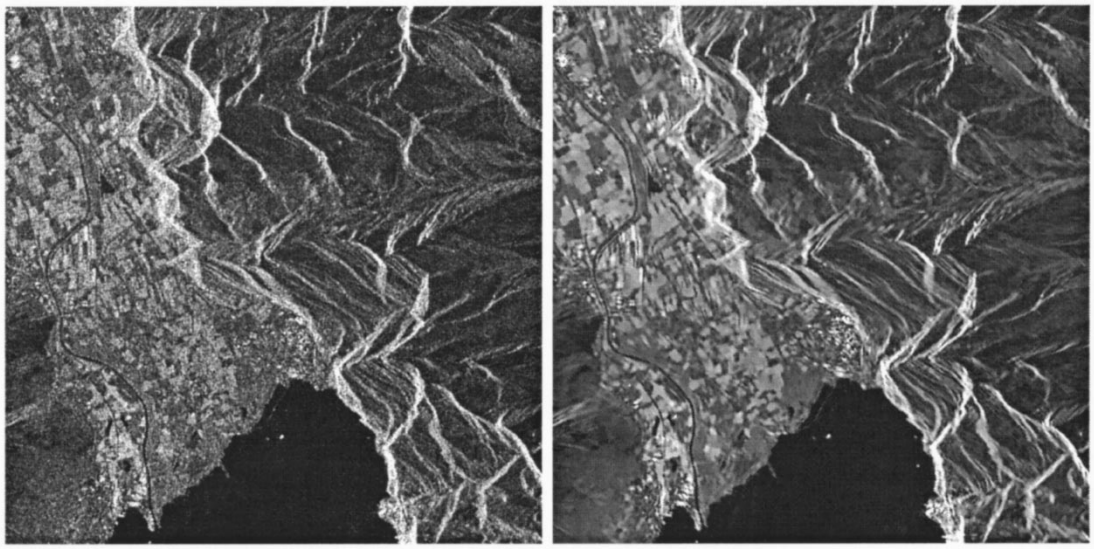

Fig. 15. X-SAR example 1, Left: Original X-SAR image (ENL $= 3.5$, 512×512 pixels). Right: Despeckled image obtained with the described algorithm (ENL $= 122$).

The presented filter not only produces a despeckled image but also provides additional information in form of texture parameters, a scatterer, and an edge map. As demonstrated, these features are well suited for further image interpretation. This is especially important, as the number of SAR sensors for high resolution imagery is steadily demanding new interpretation tools

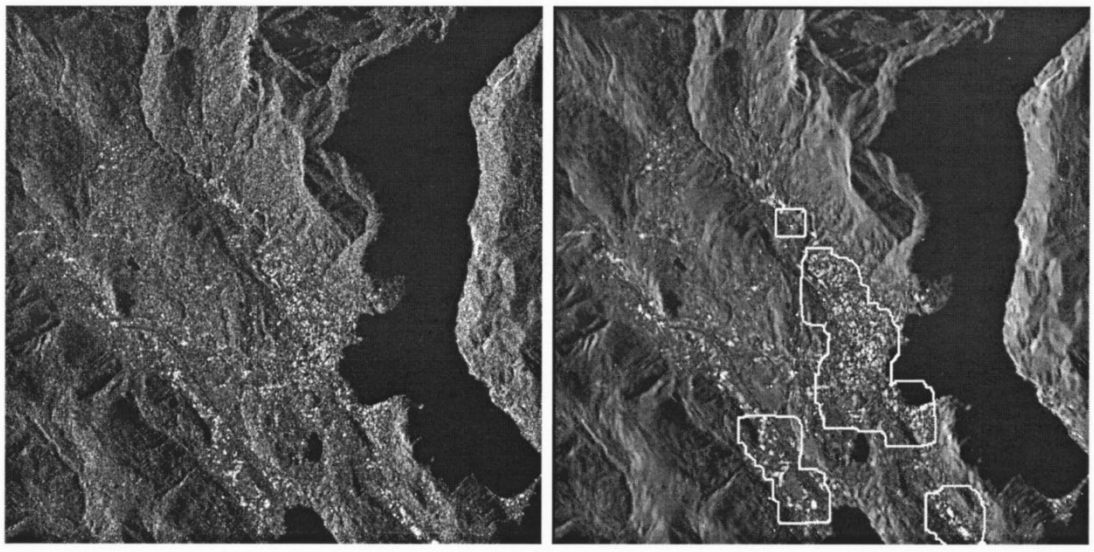

Fig. 16. X-SAR example 2, Left: Original X-SAR image (ENL $= 3.5$, 512×512 pixels). Right: Despeckled image using the described algorithm (ENL $= 371$). Marked regions are urban areas obtained by thresholding the density of detected point targets.

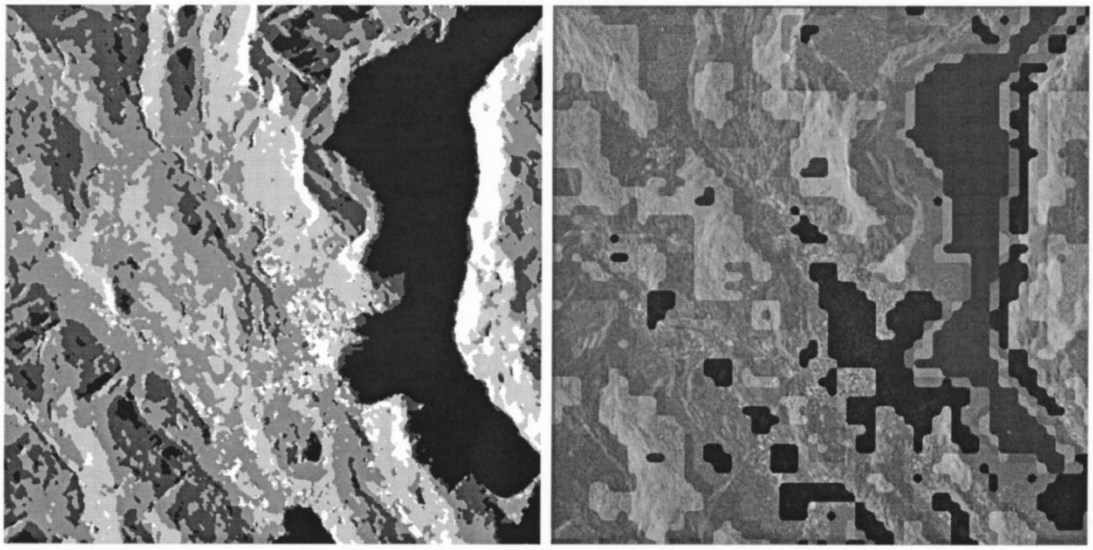

Fig. 17. X-SAR example 3: Left: Global backscatter segmentation of original data into five classes using the described region growing technique. Right: Clustering of the norm $|\boldsymbol{\theta}|$ of the extracted parameters into five classes (lake, city, valley, higher mountains, and lower mountains).

and new image archiving systems based on retrieval by image-content techniques. We think that one step in this direction has been made with the proposed approach, whose output can be used directly in such systems [19].

ACKNOWLEDGMENT

The authors would like to thank F. Faille for her help and for her suggestions concerning the manuscript.

REFERENCES

[1] R. E. Blahut, *Principles and Practice of Information Theory*. Reading, MA: Addison-Wesley.

[2] R. Cook, I. McConnell, D. Stewart, and C. Oliver, "Segmentation and simulated annealing," *Satellite Remote Sensing III*, Sept. 1996.

[3] M. Datcu, K. Seidel, and M. Walessa, "Spatial information retrieval from remote sensing images—Part I: Information theoretical perspective," *IEEE Trans. Geosci. Remote Sensing*, vol. 36, pp. 1431–1445, Sept. 1998.

[4] H. Derin and H. Elliott, "Modeling and segmentation of noisy and textured images using Gibbs random fields," *IEEE Trans. Pattern Anal. Machine Intell.*, vol. PAMI-9, pp. 39–55, Jan. 1987.

[5] S. Geman and D. Geman, "Stochastic relaxation, Gibbs distributions and the Bayesian restoration of images," *IEEE Trans. Pattern Anal. Machine Intell.*, vol. 6, pp. 721–741, Nov. 1984.

[6] D. Geman, *Random fields and inverse problems in imaging*. Berlin, Germany: Springer-Verlag, 1988, pp. 117–193.

[7] J. W. Goodman, "Statistical properties of laser speckle patterns," in *Laser Speckle and Related Phenomena*, J. C. Dainty, Ed. Berlin, Germany: Springer-Verlag, 1975.

[8] W. Hagg and M. Sties, "Efficient speckle filtering of SAR images," *Proc. IGARSS '94*, vol. 4, pp. 2140–2142, 1994.

[9] S. Lakshmanan and H. Derin, "Simultaneous parameter estimation and segmentation of Gibbs random fields using simulated annealing," *IEEE Trans. Pattern Anal. Machine Intell.*, vol. 11, pp. 799–813, Aug. 1989.

[10] J.-S. Lee, "Speckle supression and analysis for synthetic aperture radar images," *Opt. Eng.*, vol. 25, no. 5, pp. 636–643, May 1986.
[11] W. von der Linden, R. Preuss, and V. Dose *et al.*, "The prior-predictive value: A paradigm of nasty multidimensional integrals," in *Maximum Entropy and Bayesian Methods*, W. von der Linden *et al.*, Eds. Norwell, MA: Kluwer, 1999, pp. 319–326.
[12] A. Lopez, E. Nezry, R. Touzi, and H. Laur, "Structure detection and statistical adaptive speckle filtering in SAR images," *Int. J. Remote Sensing*, vol. 14, no. 9, pp. 1735–1758, 1993.
[13] D. J. C. MacKay, "Bayesian interpolation," *Neural Comput.*, vol. 43, 1992.
[14] N. Metropolis, A. W. Rosenbluth, M. N. Rosenbluth, A. H. Teller, and E. Teller, "Equations of state calculations by fast computing machines," *J. Chem. Phys.*, vol. 21, pp. 1087–1091, 1953.
[15] C. J. Oliver, "Information from SAR images," *J. Phys. D: Appl. Phys.*, vol. 24, pp. 1493–1514, 1991.
[16] C. J. Oliver, A. Blake, and R. G. White, "Optimum texture analysis of synthetic aperture radar images," in *Proc. SPIE*, vol. 2230, 1994, pp. 389–398.
[17] A. H. Schistad Solberg and A. K. Jain, "Texture fusion and feature selection applied to SAR imagery," *IEEE Trans. Geosci. Remote Sensing*, vol. 35, pp. 475–479, Mar. 1997.
[18] M. Schroeder, H. Rehrauer, K. Seidel, and M. Datcu, "Spatial information retrieval from remote sensing images—Part II: Gibbs Markov random fields," *IEEE Trans. Geosci. Remote Sensing*, vol. 36, pp. 1446–1455, Sept. 1998.
[19] M. Schroeder and H. Rehrauer. (1999). [Online] Available: http://www.dfd.dlr.de/srtm/html/data_minigen.htm.
[20] D. S. Sivia, *Data Analysis: A Bayesian Tutorial*. Oxford, U.K.: Clarendon, 1996.
[21] M. Walessa and M. Datcu *et al.*, "Texture reconstruction in noisy images," in *Maximum Entropy and Bayesian Methods*, W. von der Linden *et al.*, Eds. Norwell, MA: Kluwer, 1999.
[22] M. Walessa, "Texture preserving despeckling of SAR images using GMRFs," *Proc. IGARSS 99*, vol. 3, pp. 1552–1554, 1999.
[23] ——, "Bayesian information extraction from SAR images," Ph.D. thesis, Univ. Siegen, Siegen, Germany, submitted for publication.
[24] G. Winkler, *Image Analysis, Random Fields and Dynamic Monte Carlo Methods: A Mathematical Introduction*. Berlin, Germany: Springer-Verlag, 1995.

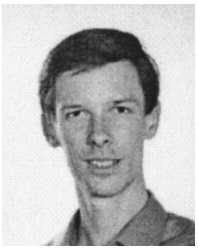

Marc Walessa received the degree in electrical engineering and telecommunications from Rheinisch-Westfälische Technische Hochschule Aachen (RWTH), Aachen, Germany, in 1996, working in the signal theory group of the telecommunications institute. He is currently pursuing the Ph.D. degree at the German Remote Sensing Data Center, German Aerospace Center (DLR/DFD), Oberpfaffenhofen, Germany, working on Bayesian SAR data interpretation and speckle filtering

In 1995, he joined the Image Processing Department, Ecole Nationale Supérieure des Télécommunications (ENST), Paris, France, for a six-month project work on stereovision. His research interests are in image and speech processing and information theory.

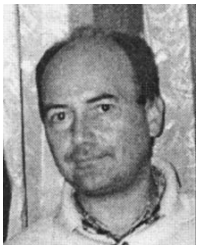

Mihai Datcu received the Ph.D. degree in electronics and telecommunications from the University "Polytehnica," of Bucharest (UPB), Bucharest, Romania, in 1986, and the title "Habilitation à diriger des recherches" from the Université Louis Pasteur, Strasbourg, France, in 1999.

He has held an image processing Professorship with UPB since 1981. He was a Visiting Professor from 1991 to 1992 with the Department of Mathematics, University of Oviedo, Oviedo, Spain, and from 1992 to 1993, 1996 to 1997, 1998, and 2000, was with the Swiss Federal Institute of Technology (ETH), Zürich, Switzerland. In 1994, he was Guest Scientist with the Swiss Center for Scientific Computing (CSCS, Manno, Switzerland. He was teaching stochastic image analysis, fractal analysis, image processing in medical sciences, and designing and developing new concepts and systems for image information mining, realistic visualization, query by image content from very large image archives, and new algorithms for parameter estimation. Since 1993, he has been a Scientist with the German Remote Sensing Data Center (DFD), German Aerospace Center (DLR), Oberpfaffenhofen, Germany. He is developing algorithms for scene understanding from synthetic aperture radar (SAR), and interferometric SAR data, model-based methods for information retrieval, and conducts research in information theoretical aspects and semantic representations in advanced communications systems. Currently, he is Image Analysis Group Leader, Remote Sensing Technology Institute (IMF), (DLR). His interests are in Bayesian inference, information theory, stochastic processes, model-based scene understanding, image information mining with applications in information retrieval and understanding of high resolution SAR and optical observations.